




Application of Electrical Resistivity Tomography for Investigating the Internal Structure and Estimating the Hydraulic Conductivity of In Situ Single Fractures

ZHEN SONG,¹  QI-YOU ZHOU,¹ DE-BAO LU,^{2,3} and SEN XUE¹

Abstract—Fractures greatly impact the hydraulic and mechanical characteristics of fault zones; thus, the hydraulic characteristics of single fractures are critical for better understanding the hydrology of regional fault zones. A number of geophysical methods are applicable on the in situ field measurement scale. Electrical resistivity tomography (ERT) is a sensitive and nondestructive approach capable of imaging the spatiotemporal resistivity variations within a fractured medium. In this study, we conducted two water infiltration monitoring experiments along in situ single fractures within tight rock using the ERT method. First, we constructed a three-dimensional (3-D) variable-density model subdivided into tetrahedra identical to the in situ fracture and verified the feasibility and accuracy of the fracture-tracking ERT (FT-ERT) through numerical simulations. Second, based on the verification of FT-ERT, the fracture resistivity variations were obtained, and the spatial and temporal variations in electrical resistivity inside the fracture were used to delineate the internal water infiltration fronts. Finally, we depicted the infiltration fronts, calculated the water infiltration velocity, and estimated the fracture permeability. The electrical response characteristics of the fractured medium revealed obvious preferential flow during infiltration. Moreover, the results indicate that the internal structure of field fractures is discontinuous and heterogeneous and that FT-ERT monitoring can not only effectively capture the spatial structures of subsurface fractures but also provide quantitative data for assessing the water conductivity of discontinuous media with strong spatial anisotropy and heterogeneity. Studying the internal hydraulic characteristics of fractures is particularly valuable for understanding the water-conducting and water-resistive characteristics of fault zones.

Keywords: Fractured rock, electrical resistivity tomography, spatial structure, hydraulic conductivity, preferential flow, heterogeneous permeability.

1. Introduction

Fractures are usually found at deep depths within tight rocks. This makes it difficult to locate them from the surface. For natural fractures, they are not parallel plates, as assumed in some theoretical studies (e.g., Houseworth et al., 2013; Huang et al., (2021), but consist of uneven rock surfaces, and thus often have a complex internal structure. If they were filled with water, these complex internal structures would determine the flow paths, greatly affecting the hydraulic characteristics of fractures. Therefore, understanding the complex internal structure of fractures has become a major concern for hydrologists and geologists (Andrade & Rangarajan, 2019). In the field of high-level radioactive nuclear waste geodisposal, this is especially important, because leaked nuclear waste may diffuse into the fracture interior, and the fate of waste there needs to be ascertained (Wang et al., 2018). Therefore, a proper understanding of the internal structure of fractures also helps us describe the hydraulic characteristics in fractured rocks.

For the natural fractures in the subsurface, the internal structure possesses enormous variations in its morphology, which includes the geometry, topology, and roughness of the contact surface. The geometry refers to the size or aperture of fractures as well as their shape. The topology describes the connection relationship of each two surfaces of fractures (Sahimi, 2011). The roughness of the contact surface

¹ School of Earth Sciences and Engineering, Nanjing University, 163 Xianlin Road, Nanjing 210023, Jiangsu, China. E-mail: song_zhen@smail.nju.edu.cn; zhouqy@nju.edu.cn; studybrother@smail.nju.edu.cn

² Key Laboratory for Technology in Rural Water Management of Zhejiang Province, Zhejiang University of Water Resources and Electric Power, 583 Xuelin Road, Hangzhou 310018, Zhejiang, China. E-mail: ludb@zjweu.edu.cn

³ College of Water Conservancy and Environmental Engineering, Zhejiang University of Water Resources and Electric Power, 583 Xuelin Road, Hangzhou 310018, Zhejiang, China.

affects the hydrodynamic and mechanical behaviour of fluid flow (Suri et al., 2020). Many methods and techniques have been utilized to describe and quantify the morphology of the surface structure, including the fractal concepts (Tayfun et al., 2015), the 3-D stereo-topometric measurement (Nasseri et al., 2010), and the high-resolution structure from motion photogrammetry (Zambrano et al., 2019). These experimental and technical developments are fully capable of precisely identifying the fracture surfaces of rock samples. However, there is still a lack of adequate technical means to characterize the internal structure of fractures buried in the subsurface. Thus, an effective method that can reveal the spatial distribution of fractures, monitor the fluid flow within fractures, and evaluate the hydraulic characteristics of single fractures in the field is vitally needed.

A clear understanding of internal structure is key for efficient evaluation of hydraulic characteristics. Many researchers have studied the hydraulic characteristics of fractured rocks using classic and innovative techniques. For example, to analyze the mechanical and hydraulic properties of fractured media, Kuhlman et al. (2015) proposed multi-porosity fractured rock flow models. Rashid et al. (2015) suggested a model based on the Revil, Glover, Pezard and Zamora (RGPZ) theoretical model (as coined by Glover et al., 2006) to reliably predict permeability in tight carbonates. Song and Zhou (2019) used an image analysis method to quantify the parameters of microcracks in granite and conducted lattice Boltzmann method (LBM) simulations to determine the permeability of fractures. Zambrano et al. (2019) analyzed the fracture roughness control on permeability using structures from motion photogrammetry and fluid flow simulations.

Nevertheless, most investigations of fractured media have focused only on fracture networks (Hadgu et al., 2017; Wang (2019)) or on their simulation (Yan et al., 2018; Zou et al., 2017). Furthermore, in most cases, researchers studied the fractures in field scale only as a whole rather than analyzing the influence of a single fracture on the percolation process. However, single fractures play a vital role in the water conductivity characteristics of fractured media. In reality, a variety of factors,

including the lithological characteristics of the surrounding rock and the filling materials and geometric features of fractures, contribute to the heterogeneous characteristics of single fractures.

The heterogeneity of groundwater flow in fractured media manifests in two main aspects: lithological differences and structural differences. Lithological differences refer to the preferential infiltration caused by the different physical characteristics of the fractured rock, whereas structural differences refer to the preferential infiltration caused by the existence of faults or fractures in a rock mass (Hyman et al., 2019). The former generally have larger spatial distributions and are easy to identify; in contrast, the spatial distributions and hydraulic characteristics of fractures (structural differences) in rock masses are difficult to ascertain due to their small spatial extent (Bodin et al., 2003). Consequently, it is both critical and difficult to relate the hydraulic conductivity in a fractured medium to its properties. For this reason, field measurements such as core logs (Herron, 1988), geophysical logs (Tsang and Doughty, 2003), pumping tests (Walton, 1990), and water pressure tests (Suski et al., 2004) are commonly carried out during petroleum exploration. Brooks and Corey (1966), van Genuchten (1980), and Fredlund and Xing (1994) have conducted considerable work in this field; their experiences and methods are broadly used to directly study the unsaturated permeability of rock fractures.

As to the fractures in the field, there are fundamental differences in the internal structure and hydraulic characteristics. These differences lead to the various permeability distribution characteristics. However, the ability to accurately characterize the unsaturated permeability of fractures is limited because the unique structural features of fractures cannot be easily determined (Robinson et al., 2016). For this reason, electrical resistivity tomography (ERT) may be a better option for accomplishing this task, as it is a sensitive, effective, and nondestructive technique for acquiring details about the subsurface geological setting (Binley & Kemna, 2005). Therefore, the goal of this study is to characterize the internal structure and heterogeneity of single fractures using the ERT technique (Sreeparvathy et al., 2019).

ERT is a well-established geophysical technique (Loke et al., 2013; Zhou et al., (2004) based on the theory of the electrostatic field and the premise of detecting the electrical differences of the target (Travelletti et al., 2011). When there is a difference in the electrical properties between the detected object and the surrounding medium, ERT can effectively map the spatial distribution of the detected object (Ronczka et al., 2015). At the field level, ERT provides a good view of the connectivity of fractured zones (Lu et al., 2021). In addition, ERT monitoring is sensitive to the composition of fracture infill, which provides the possibility for the spatiotemporal imaging of fluid transport. Furthermore, a pseudosection resistivity data set can be inverted by an appropriate inversion method to image the internal structure of fractures (Binley & Kemna, 2005). However, while many numerical simulations of fracture models have been presented (Noiriel et al., 2013; Hyman et al., (2019), few in situ experiments have been conducted using the ERT method for a single fracture, and thus there is a paucity of experimental data on the permeability distribution in the interior of a single fracture. Abdelazim (2016) presented an approach on glass bed models with a single fracture to simulate the fluid flow in an unsteady state and estimated the relative permeability curve. LaBrecque et al. (2004) demonstrated that ERT can correctly locate resistive fractures in experiments on dry (resistive) and wet (conductive) fractures. Their results confirmed that conductive fractures yield smaller responses than resistive fractures, which has important implications in the current study for assessing the internal structure of fractures. The work of Ochs and Klitzsch (2020) illustrated the influence of electrodes on measurement resolution based an analysis of a three-dimensional (3-D) ERT model, and also indicated that researchers should test its validity by modeling. In the optimized survey design of Uhlemann et al. (2015), the results obtained by simulating a single line of electrodes reflected the locations of subsurface anomalies with high resolution. All these studies prove the feasibility of using the ERT method to detect fracture anomalies.

This study proposes a monitoring method employing fracture-tracking ERT (FT-ERT) on an outcrop with single fractures to identify the primary

hydrogeological heterogeneity in the interior of the fractures. The validity of a 3-D synthetic model composed of a single fracture and the surrounding rock mass is tested to determine the effectiveness of FT-ERT for this kind of research. By setting up different anomalies with different resistance, we simulate and invert the data corresponding to different field situations. Subsequently, we perform two FT-ERT infiltration experiments in two in situ fractures. The experimental objects are a single fracture and crossing fractures, respectively. Based on the validation of the model, we construct resistivity pseudosections from the inverted data to understand the inner properties of the fracture. Moreover, we depict the dominant water pathways and characterize the spatial and temporal development of water migration. The specific contours of the relative variation in resistivity, which indicate the infiltration fronts of preferential flow (Robinson et al., 2016), are extracted and drawn to highlight the variance of the infiltration velocity. Finally, we estimate the permeability and analyze the heterogeneity of the single fracture and crossing fractures.

2. Methodology

2.1. Fractures Selected for the Experiments

The experimental site in this study is located in Beishan, Gansu Province, northwestern China, where various granite outcrops and observable fractures are widely distributed on the surface (see Fig. 1a, b). We selected two shear fractures, which we refer to as the single fracture (Fig. 1b) and the crossing fractures (Fig. 1c), to conduct the monitoring experiments.

The orientation (strike) of the single fracture is $NE15^\circ$. Based on observations with the naked eye, the single fracture can be simplified as a relatively simple vertical plane that intermittently reaches the ground surface. Its trace extends over 10 m, and the maximum aperture reaches 1 cm. Visible filling materials are weathered silt, fine sand, and silty clay. The crossing fractures are formed by two shear fractures intersecting one another at their midpoints at an angle of 76° . A Cartesian coordinate system was adopted in the experiment. We defined the east–west

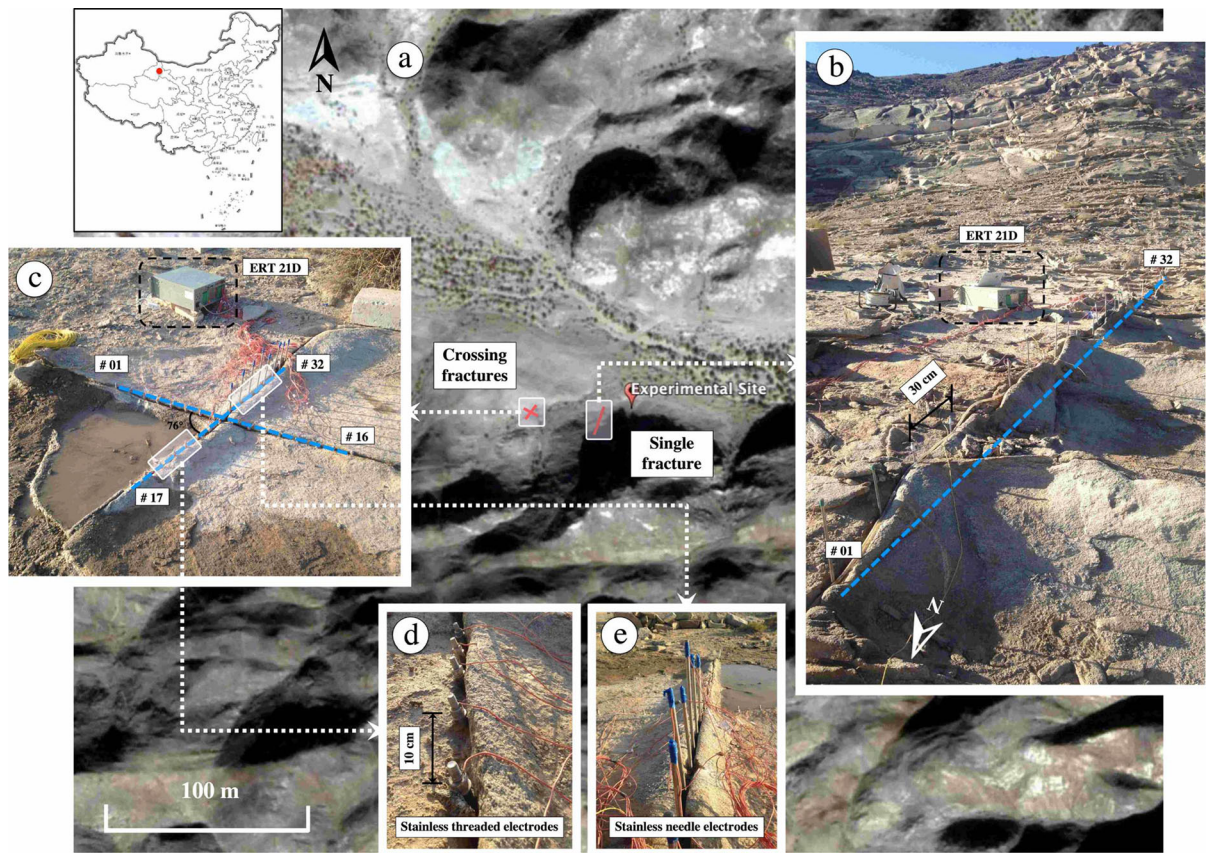


Figure 1

Location of the experimental site. The main host rock in this research area (a) is granite. Single fracture (b) and crossing fractures (c) are located south of a fault zone. Stainless threaded electrodes (d) and needle electrodes (e) were installed along the fractures with different spacing intervals

direction of fracture extension as the X -axis. The intersection point was on the X -axis and was 0.75 m from the origin. The lengths of the fracture outcrops in the X - and Y -direction (approximate) were 2.25 m and 1.92 m, respectively. Viewed from the ground surface, the filling materials were not visible. The crossing fractures were located 14.3 m to the west of the single fracture, and both were subordinate to the same large fault (F4). The rock surrounding these two fractures had the same physical properties.

To gain insight into the nature of the fractures, we conducted a borehole sampling (for surrounding rock) and soil analysis (for filling materials) of the fractures. A 56 mm-diameter borehole was drilled close to the intersection to fully assess the physical properties of the surrounding rock. The borehole

analysis results showed that the permeability of the surrounding rock medium was $5.56 \times 10^{-18} m^2$, the total density was $2.69 g/cm^3$, and the connected porosity was 1.2%, indicating a low-permeability medium. Petrographic analysis revealed that the core samples were biotite plagiogneiss. The filling materials in the fracture interior were mainly composed of fine sand, with a particle size from 0.16 to 0.42 mm.

2.2. FT-ERT Measurements

Two FT-ERT experiments were conducted in the study area using a pole-pole configuration. We arranged 32 stainless electrodes (Fig. 1d, e) within the fractures encountered at the outcrops. The electrode arrangement in the single fracture is shown

in Fig. 2. The electrode spacing between nearby electrodes was set to 0.3 m. The electric current and potential remote electrodes were set at 8 m and 10 m from each end of the fracture trace, respectively. With this arrangement of 32 electrodes, 265 records were collected at each scanning measurement, with each scanning measurement taking approximately 42 min. Each record includes voltage, current, resistance and chargeability.

For the crossing fractures, a total of 16 electrodes were installed in each fracture, and the electrode spacing was set to 0.1 m. Because of the small aperture of the crossing fractures, threaded electrodes were utilized to replace the stainless electrodes applied in the single fracture experiment. The total length of each threaded electrode was 7.5 cm, and the depth of insertion into the fracture was 3 cm. The electric current and potential remote electrodes were arranged 10 m to the north and south of the crossing point, respectively (see in Fig. 1c). Measured records in the *X*- and *Y*-direction were obtained in each scanning measurement. The time for each measurement was approximately 34 min, and the measurement interval was 3–5 s.

In the process of these two infiltration monitoring experiments, the electrodes were then connected to an ERT21 measurement system (model ERT21D, Nanjing Geozhou Exploration Technology Company Ltd, Nanjing, China). By sequentially switching on the electrodes given in a protocol file, the system can

make automatic resistivity scanning measurements at every given time. Thus, resistivity variations in space and time were monitored.

2.3. Water Infiltration Experiments on the Fractures

We developed a linear uniform water infiltration apparatus to monitor percolation processes along a horizontal profile (in Fig. 2). The infiltration apparatus is equipped with a constant-head reservoir and an outlet pipe port, which allows a constant head to be maintained during the test. The outlet pipe is a perforated water pipe laid across the entire fractured outcrop during the monitoring process. The spacing of the holes in the pipe is 1 cm to ensure that the amount of water leakage remains the same. Because of the water head pressure of the pipe, the water evenly infiltrates the whole fracture, as shown in Fig. 2. Over 40 L of water was injected into the fractures in two experiments. However, considering the leakage of water, the actual amount of water that entered the fracture was less than 40 L.

2.4. Relationship Between Resistivity and Water Content

The hydraulic parameters of the fractured medium in this paper are represented by the distribution of electrical properties affected by the water content.

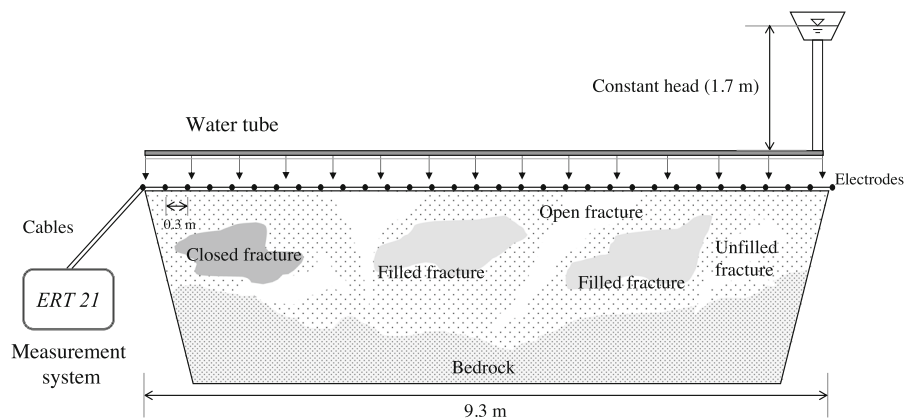


Figure 2
Schematic diagram of the water infiltration and ERT monitoring instruments

Our method for obtaining the hydraulic parameters is based on Archie's relationship (Archie, 1942):

$$\rho = \rho_w \varphi^{-\alpha} S_w^{-\beta}, \quad (1)$$

where φ denotes the porosity, $S_w = (\theta - \theta_r)/(\theta_s - \theta_r)$ is the effective saturation, ρ is the resistivity of the porous medium (Ωm), and ρ_w is the resistivity of the porous medium (Ωm) when the water saturation is $S_w = 1$. α is the cementation exponent (usually in the range of 1.8–2.0 for sandstones), and β is the saturation exponent (usually close to 2). θ is the water content (cm^3/cm^3). θ_s and θ_r are the saturated and residual water content, respectively. According to Eq. 1, the relationship between the water content and resistivity values is nonlinear. The medium resistivity ρ has a decreasing trend as the water content θ_s gradually increases. This trend can provide more intuitive evidence for determining the spatial location of infiltrating water.

3. Numerical Verification of the Effectiveness of FT-ERT in the Investigation of the Fracture Internal Structure

3.1. Forward modeling

Forward modeling can be used to simulate real measurements collected by machines, potentially providing a powerful capability to investigate problems such as the responses of the measurement network to a target and its resolution. For a 3-D homogeneous medium, given a point source in an idealized space, the electric potential ϕ at a distance \mathbf{r} from the point can be defined by Poisson's equation:

$$\nabla \cdot \sigma \nabla \phi = -I \delta(\mathbf{r}), \quad (2)$$

where σ is the subsurface electric conductivity and δ is the Dirac delta function. For a half-space medium, the potential can be expressed as $\phi = \rho I / 2\pi r$, where ρ is the resistivity. The ground surface is commonly used as a zero-flux boundary, while the other boundaries are given. The potential value of the analytical solution under homogeneous conditions is selected as the value of the given boundary. For a point electrode located at (x_0, y_0, z_0) , $\delta(\mathbf{r})$ becomes $\delta(x - x_0)\delta(y - y_0)\delta(z - z_0)$. For the forward modeling

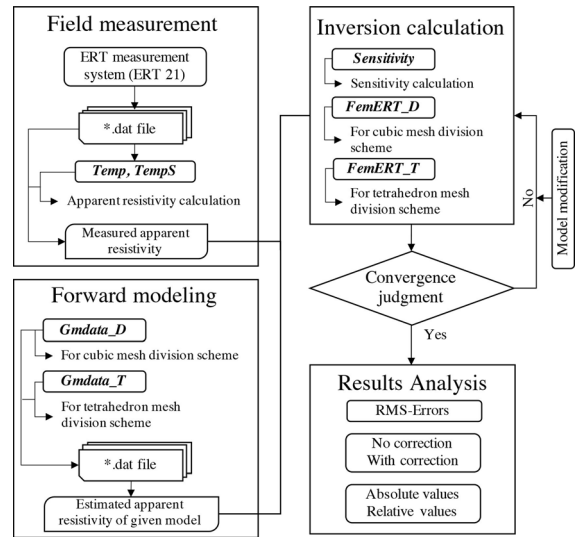


Figure 3

Flow diagram of electrical resistivity data processing. *Temp* and *TempS* are programs used to calculate the resistivity of the measured data. *GmData_D* and *GmData_T* are forward modeling programs for cubic blocks and tetrahedrons as elements, respectively. *Sensitivity* is a program used to calculate the sensitivity matrix before the inversions. *FemERT_D* and *FemERT_T* are inversion programs for cubic blocks and tetrahedrons as elements, respectively

in this study, the finite element method (FEM) is used, considering its flexibility in selecting elements. According to the minimum theorem, solving Eq. 2 is equivalent to minimizing the functional:

$$F(\phi) = \sum_j \int_{V_j} [\sigma_j (\nabla \phi)^2 - 2\phi \nabla \cdot I \delta(x - x_0)(y - y_0)(z - z_0)] dV_j. \quad (3)$$

In this study, we used the *GmData_T* (Fig. 3) program by Zhou et al. (1999) to accomplish the forward calculation. A tetrahedron division scheme was adopted.

3.2. Inversion Algorithm

To obtain a map of the 3-D resistivity distribution within the medium from a large amount of apparent resistivity data, it is necessary to carry out an inversion to obtain the best possible results. The FT-ERT method enhances the reliability of the inversion results by obtaining a large amount of data. To modify the model, the patching method proposed

by Zhou et al. (1999) was adapted to the pole–pole configuration, and the *FemERT_T* program developed by Zhou et al. (1999) was utilized for the inversion.

This program is based on maximum likelihood inverse theory (MLIT), which provides the best fit to the data relative to a priori information. For the pole–pole measurements, all of the measurements with the same current electrode and same input current are defined as one measurement event. For each event, only one calculation of the forward problem is needed to obtain the potential. If there are m_i measurements or receivers for event i , then m_i potential differences between the modeled and measured data can be obtained, and the sensitivity matrix S^i of event i has only $m_i \times s$ elements. According to Tarantola and Valette (1982), the perturbation $\Delta\rho$ is linearly related to the potential difference. On the other hand, the perturbation $\Delta\rho_j$ at element j is also related to the sensitivity of different receivers at this element: the larger the sensitivity, the greater the perturbation resulting from this receiver. Thus, the perturbation $\Delta\rho_{kj}^i$ at element j resulting from the k th receiver of event i can be expressed as

$$\Delta\rho_{kj}^i = S_{kj}^i \Delta d_k^i \quad (k = 1, 2, \dots, m_i; j = 1, 2, \dots, s), \quad (4)$$

where s is the total element number. The $\Delta\rho_j^i$ should be the sum of perturbations from different receivers:

$$\Delta\rho_j^i = \sum_{k=1}^{m_i} \Delta\rho_{kj}^i = \sum_{k=1}^{m_i} S_{kj}^i \Delta d_k^i \quad (j = 1, 2, \dots, s). \quad (5)$$

As a result, the perturbation vector $\Delta\rho^i$ from event i can be obtained, and $\Delta\rho^i$ can be added to the initial model parameters to update the model parameters after applying a smoothing filter. Then, the perturbation of the model parameters can be repeated for the next event. The resistivity data are sequentially updated by using the measured data from each event in the same method. One cycle of events constitutes one inversion iteration.

This procedure is repeated until the misfit between the total measured and modeled data is reduced to an acceptable root-mean-square (RMS) level. This algorithm is used to calculate the

perturbations considered for each measurement event, thus accommodating the resistivity change between measurement events. For every measurement event independently contributing to improving the model parameters, it is appropriate to use measurement instruments with different numbers of channels and different measurement objectives. Because the perturbation vector $\Delta\rho^i$ given by Eq. 5 is large near electrodes and gradually decreases to zero with increasing distance from the electrodes, the perturbation resulting from each event is similar to a patching process, so this technique is called the patching method.

3.3. A Comparison of the Inversely Calculated Tomography with that of the Resistivity Model

In many cases, the resistivity profiles cannot directly represent the geometry of anomalies, due to the small difference between the resistivity of the objective and the background (Dumont et al., 2018). Time-lapse FT-ERT data are interpreted in terms of relative changes in electrical resistivity. We calculated the relative variation in the apparent resistivity (r_ρ) by the following equation:

$$r_\rho = \frac{\rho_a - \rho_b}{\rho_b} \times 100\%, \quad (6)$$

where the ρ_a is the resistivity of the model (with anomalies), and ρ_b is the resistivity of the background (without anomalies).

As shown in Fig. 4, the numerical model is the same size as the single fracture in the field; additionally, the same measurement method is applied with the same electrode combination. The length of the model is 11.4 m, and the width is 2 m. In the middle is a fracture with a width of 5 cm. Two cylindrical anomalies, one with high resistivity (3500 Ωm) and one with low resistivity (150 Ωm), are buried at a depth of 2.25 m. Both anomalies are located in the fracture area with a width of 5 cm. The radius of each cylindrical anomaly is 1 m. The research area is in an arid environment that receives very little precipitation (60–80 mm/year). The interiors of field fractures are often filled with dry fine sand and silt. Because of these conditions, the background resistivity of the surrounding rock and

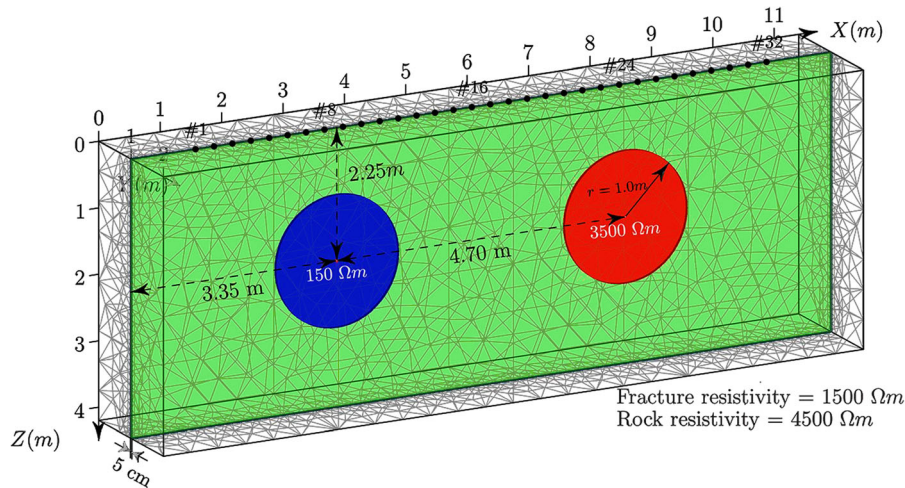


Figure 4

Synthetic model composed of variable-density tetrahedrons. A parallel-plate model of the fracture is set up with a high-resistivity background. Two cylindrical anomalies are contained in the fracture area with a width of 5 cm

fracture area is set as $4500 \Omega m$ and $1500 \Omega m$ (MacNeill 1980), respectively. We assumed 32 electrodes in a straight line with a spacing of 0.3 m. Synthetic apparent data generated with a pole-pole configuration were used as raw data for the inversion.

To verify that *Gmdata_T* and *FemERT_T* are reliable for 3-D modeling and inversion, the analytical results and boundless ERT (BERT) (Rücker et al., 2006; Günther et al., 2006) forward and inverse

modeling were adopted for comparison. We selected the X-Z section of the model ($y = 0m$) to compare the simulation results. Figure 5 shows the spatial distribution of the relative variation in resistivity. Figure 5a and b show the apparent resistivity results and inversion results acquired by BERT, respectively. It is obvious that the BERT numerical simulation results reveal the anomalous regions. This indicates

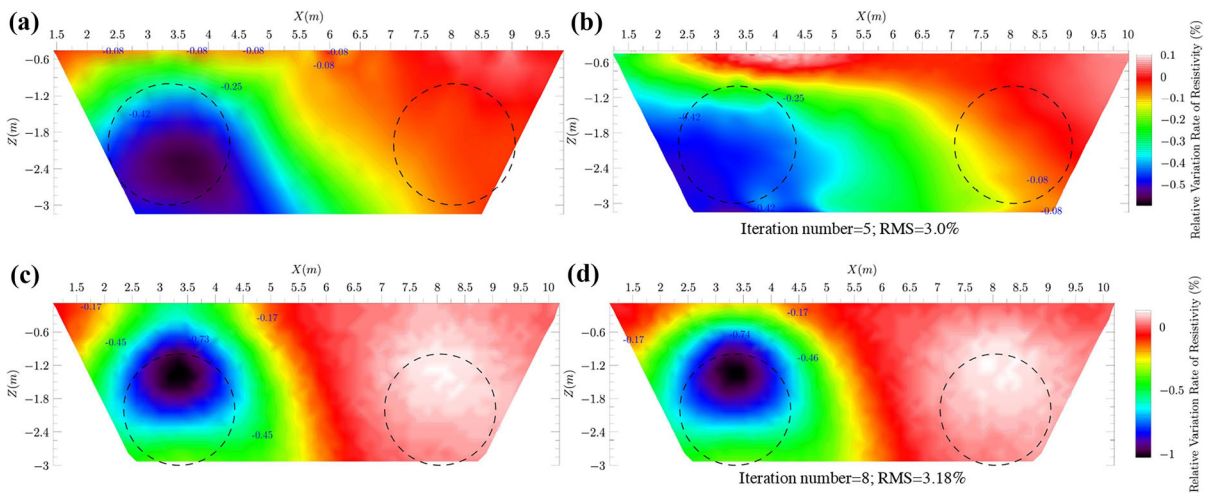


Figure 5

Numerical results expressed by the resistivity increment (the relative variation in resistivity in Eq. 6). **a** Apparent resistivity results by BERT. **b** Inversion results by BERT. **c** Apparent resistivity results by *Gmdata_T*. **d** Inversion results by *Gmdata_T*

that the detection method can be effectively used to reflect the anomalies in fractures.

Figure 5c and d present the numerical simulation results by *Gmdata_T* and *FemERT_T*. Compared with BERT, our proposed method can more clearly delineate the regional location and morphological characteristics of the anomalies. For instance, in the area of $X = 2 \sim 4m$, the contour shape of the circular anomaly is closer to the initial shape set by the model. From the data in Fig. 5d, it is apparent that the patching method has a better response to the higher-resistivity anomaly in the area of $X = 7 \sim 9m$, where the FT-ERT method has better recognition ability for deciphering the spatial structure of single fractures.

4. Experimental Verification of the Effectiveness of FT-ERT in the Investigation of the Fracture Internal Structure

4.1. Infiltration Monitoring Results for the Single

Fracture

4.1.1 Temporal Variations in Electrical Resistance in the Single Fracture

Figure 6 shows the temporal variation in the resistance corresponding to different electrode combinations (imaging points). The absolute value of $C_1 - C_2$ determines the distance from the ground surface to the imaging point. Electrode combinations such as (9, 10) and (23, 24) are close to the ground surface. In contrast, combinations such as (2, 10) and (23, 31) are at depth within the fracture. In this figure, the blue area shows the imaging points in the shallow part of the fractured medium, while the red area presents the imaging points at depth. It is clear that the shallow medium exhibits a more significant electrical response than the deep medium as a result of infiltration. The maximum variation in resistance is approximately 200Ω . Although the resistance values at (9, 10) and (23, 24) are substantially different, those at (2, 3), (30, 31), (2, 4), and (9, 10) show little change. This phenomenon indicates that the

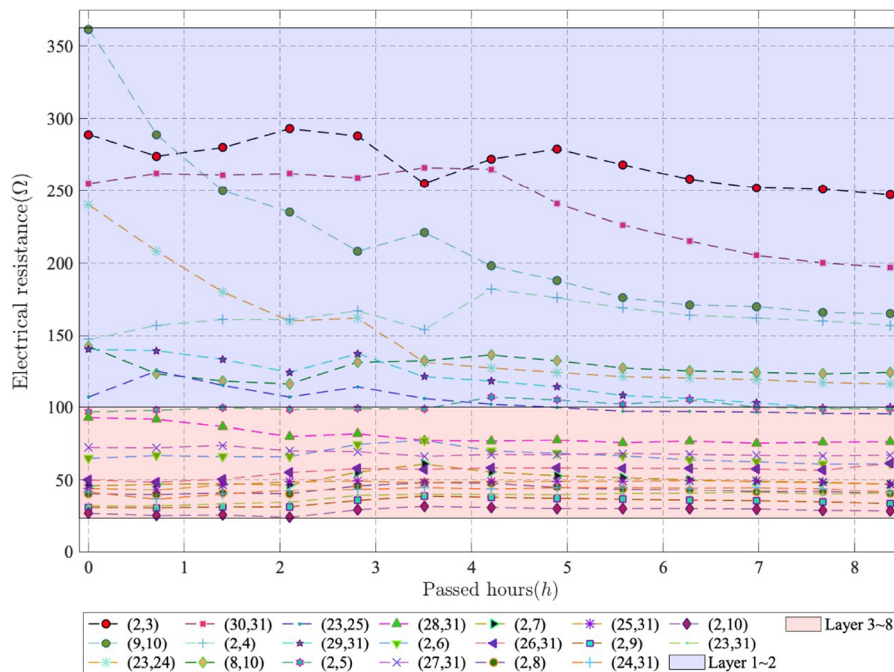


Figure 6

Temporal variations in the electrical resistance of the single fracture at 20 imaging points before and after infiltration. The imaging points are indicated by the combination of electrodes C_1 and C_2

saturation process in some areas is inhomogeneous. On the one hand, we find that the observed resistivity curves of (2, 3), (23, 24), and (30, 31) present notable fluctuations, which are attributed to partial infiltration. Nimmer et al. (2007) similarly reported that the resistivity curve does not flatten out with increasing depth in the process of water injection but fluctuates up and down. This supports the observed heterogeneity, as our results are in good agreement with their findings. On the other hand, for the combinations in the deep area, the resistivity curves only rarely fluctuate, featuring extreme variations of a few tens of ohms. The medium exhibits no strong responses caused by infiltration throughout the infiltration process. We speculate that this area may not have been affected by the infiltrated water. Another possible reason for this may be that the detection resolution was too low to recognize changes in the water content.

The temporal resistance variations can be described in stages. Generally, water movement in the fractured medium occurs in three stages: infiltration, redistribution, and drainage or deep percolation. In the infiltration stage ($t = 0 \sim 1.5h$), infiltration is defined as the initial process of water entering the medium resulting from application at the ground surface, and the resistivity curves show a universal decreasing trend. In the redistribution stage ($t = 1.5 \sim 4.5h$), drainage and wetting take place simultaneously. Drainage impacts the amount of water available for deeper penetration within the fractured medium profile. Hence, the channels or areas that show high resistance or an increase, such as (2, 3) and (2, 4), may have lost the ability to conduct water gradually. The final stage ($t > 4.5h$) of water movement is termed deep percolation, which occurs when the medium reaches a state of saturation. Dominant pathways have been established by this stage, and thus, unsaturated regions that are not conductive will not experience water recharge. An analysis of these temporal resistivity variations revealed that the water movement in the redistribution stage is inhomogeneous, thereby reflecting the heterogeneity of the fractured medium.

4.1.2 FT-ERT Results for the Single Fracture

With the aim of highlighting the structural differences, we calculated the temporal variations in inverted resistivity. We present the data for the middle section of the resistivity profile after more than 8.7 h of monitoring. The spatial distributions of the inverted resistivity and relative resistivity variation are shown in Fig. 7, which indirectly delineate the internal structure of the fracture according to Eq. 1. Figure 7a displays the resistivity results at the beginning of the experiment (before infiltration) as a background value, while Fig. 7b–d present the temporal variation in the inverted resistivity corresponding to the infiltration stage at $t = 1.39h$, $t = 2.77h$ and $t = 4.17h$, respectively. Figure 7e shows the resistivity profile when the seepage reached saturation ($t = 5.56h$). As mentioned above, the resistivity of the fractured medium gradually decreased with continuous infiltration. The decreasing trends of the resistance curves in Fig. 6 can be verified by comparing the data at four measuring times with the background.

In terms of the spatial distribution, the resistivity of the fractured medium at a given time is extremely uneven. For instance, there are two low-resistivity areas ($x = 3.7m$ and $x = 7.5m$) at a depth of 1.2 m along the X -direction. However, an area at $x = 5m$ with the same depth shows a characteristically high resistivity. The same phenomenon can be found in the deep area. At $x = 5 \sim 8.5m$ and depths greater than 1.4 m, there is a high-resistivity area, but it does not appear in the first half of this section. These findings prove that the FT-ERT monitoring method is able to reveal the complexity of internal structure. Moreover, these results are corroborated by those of Zhou et al. (2004), who found that the uneven spatial distribution of resistivity reflected the heterogeneity of the fractured medium. Their discovery further confirms the effectiveness of FT-ERT in identifying the structural differences of single fractures.

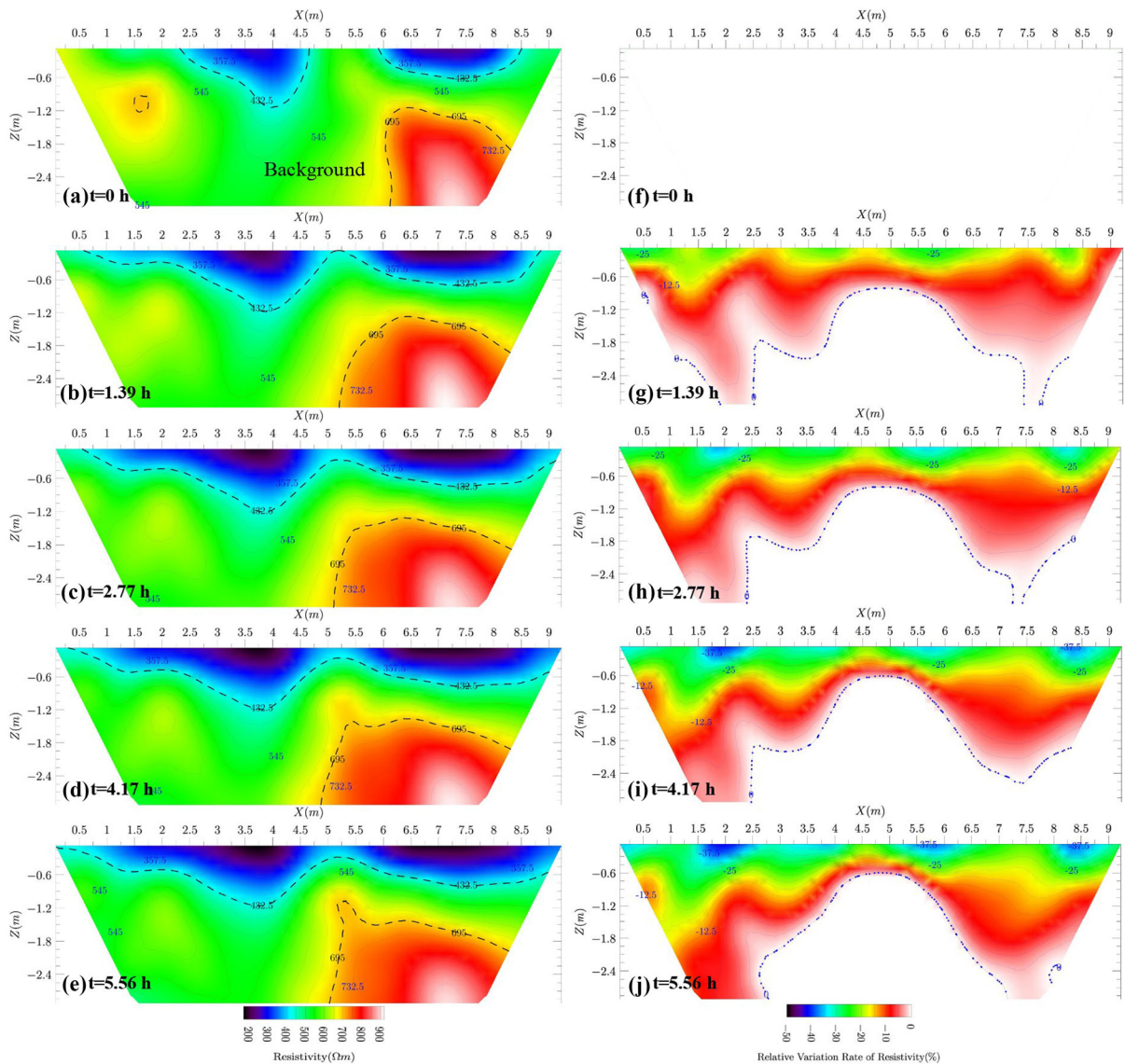


Figure 7

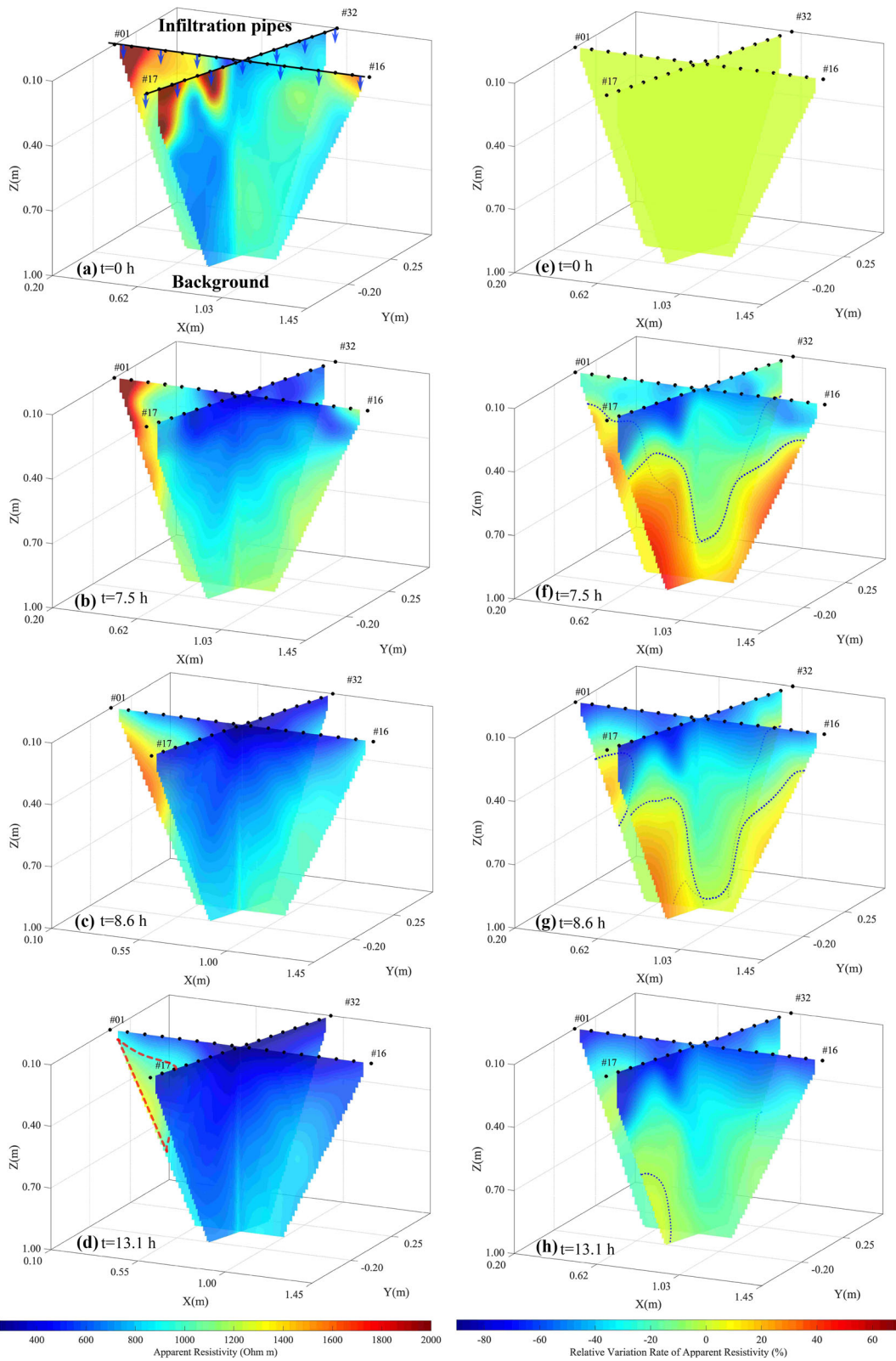
Spatial distribution of the inverted resistivity and relative variation in the inverted resistivity of a single fracture during the infiltration process

4.2. Infiltration Monitoring Results for the Crossing Fractures

In contrast to the single fracture, the crossing fractures are composed of two intersecting single fractures. We used the same method to analyze the infiltration process and percolation mechanism of the crossing fractures. The two vertically intersecting profiles in Fig. 8 present the experimental results in

the X- and Y-direction. Figure 8a shows the background resistivity at $t = 0h$, and Fig. 8b, c are the resistivity imaging results of the infiltration process at $t = 7.5h$ and $t = 8.6h$. Figure 8d illustrates the resistivity distribution of the fractures upon reaching saturation after 13.1 h of infiltration.

Fractures continuously receive water in the process of infiltration; upon being infiltrated, the resistivity of the filling materials and fracture cavities changes. By using the apparent resistivity at $t = 0h$ as



◀Figure 8

Spatial distributions of the apparent resistivity and relative variation in the apparent resistivity of the crossing fractures during the infiltration process. The blue arrows represent the deployed infiltration instruments, and the black dots are the electrodes

the background, we calculated the relative variation in apparent resistivity, as shown in Fig. 8e–h. The blue-green area in the figure indicates that the resistivity change rate is negative. The yellow-red area shows an increase in the resistivity. As can be seen in Fig. 8f and g, the dashed isolines, which have a relative variation of 0, gradually shift down in the vertical direction with continuous infiltrated water. But this trend is not synchronous horizontally. The areas of decreased resistivity at depths of 0.4–0.7 m move downward during consecutive hours and reach a steady state toward the end of the infiltration period. Eventually, the infiltration of injected water in the fracture induces maximum relative variation in resistivity of 88.23% at $t = 13.1h$ (Fig. 8h).

5. Heterogeneous Infiltration Process with Fractures Revealed by FT-ERT

5.1. Structural Heterogeneity in the Fractures

Osipov (2017) reviewed the fluid mechanics models of hydraulic fractures. Multiple factors, primarily including the filling state of the fracture and the contact relationship between the rock surfaces on both sides of the fracture, affect the structural heterogeneity of high and low resistivity within single fractures. To better understand the heterogeneity caused by structural differences, we assumed four contact relationship cases according to the fracture morphology (shown in Fig. 9). Case 1 shows the contact state of a closed fracture. The surrounding rock masses of the upper and lower walls are in close contact, and a compacted material fills the space between the fracture surfaces. Case 2 and case 3 show the most common characteristics of filled fractures. In case 2, the cavity between the fracture surfaces is completely filled with sandy soil, and thus the resistivity of the fracture comprehensively reflects the resistivity of the filling materials. In case 3, only some of the space between the two fracture surfaces contains the filling materials; we call this a partially

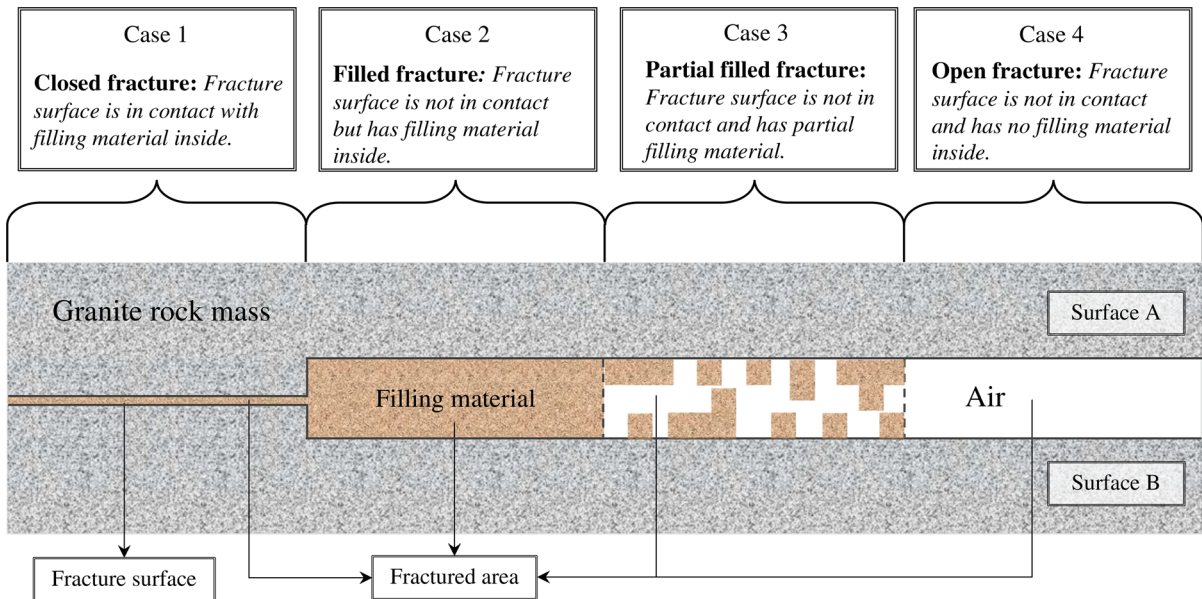


Figure 9

Schematic diagram of the internal contact and filling state of a fracture

filled fracture. The contact relationship is not parallel because the surfaces are rough; consequently, the size of the gap between the two surfaces varies. Multiple types of materials such as mud, sand, and soil are integrated with the rocks, forming a fracture model similar to an ideal fracture model composed of two parallel plates. Case 4 involves rock surfaces that are not in contact with any filling materials inside, just air; we call this an open fracture.

5.1.1 The Single Fracture

Structural Difference: Compared with the assumed model, the real internal structure of the single fracture is more complex. Assuming that the resistivity of the filling materials is lower than that of the surrounding rock, the resistivity of the fractured medium in case 1 is the lowest, while that in case 4 is the highest, and the general resistivity in case 3 is higher than that in case 2. As shown in Fig. 7a–e, it can be preliminarily concluded that the areas with resistivity below $432\Omega m$ (black dashed lines) in the center might contain infilled fractures, and thus the surfaces are in good contact (i.e., cases 1 and 2). However, the regions with resistivity above $695\Omega m$ on the right side in depth of 1.2–2.8 m might have surfaces in good contact but lack filling materials (i.e., case 4). In addition, the regions between these two contour lines might be filled with material but feature insufficient contact between the rock surfaces (i.e., case 3). Generally, there are numerous factors that can influence the resistivity of fractured medium, and inspecting the internal structure of the fracture only by the contact of the fracture surfaces is not rigorous. However, the FT-ERT method provides a simple, fast, and effective way to understand the structural heterogeneity in this way, especially for the unseen fractures underground.

Heterogeneous Infiltration: To analyze the resistivity variations induced by the water content, which is affected by the infiltrated water, we calculated and depict the relative variation in resistivity. As shown in Fig. 7 (right-hand column), the blue-green area indicates a larger resistivity change rate, while the red-white area indicates a smaller change rate. The resistivity changes are quite different, in particular at the same depth. Assuming that the filling materials of

the fracture initially have very low water content and that the water content increases with ongoing infiltration, then the resistivity differences can reflect the variations in the water content according to Eq. 1. For example, from Fig. 7g–j, the infiltration front (assumed from the resistivity variations) gradually expand with the continuous downward flow of fluid. The left and right sides are especially obvious. With continuous infiltration, the horizontal contour lines gradually curve downward on both sides of the fracture. Eventually, the contour lines became dome-like, with a positive relative variation in resistivity distributed in the central part of the dome. The water coming from the ground surface preferentially infiltrated along the two sides of the fracture. This infiltration phenomenon is probably due to structural differences in the fracture. For instance, although the lower right region of the fracture has high resistivity (refer to case 4 in Fig. 9), the medium in this region shows good hydraulic conductivity in the period of infiltration. This phenomenon suggests that the water filled the open fracture, which performed like a water conduit channel. The time-lapse images of infiltration do reflect the advance of the infiltration fronts. Furthermore, we can infer that it is possible to use the relative variation in resistivity to evaluate the heterogeneous infiltration of a fractured medium.

5.1.2 The Crossing Fractures

Structure Difference: The FT-ERT results also present the structural heterogeneity of crossing fractures. In Fig. 8, the relative variation rates reflected in the resistivity profiles show that the interiors of the two intersecting fractures are not homogeneous. Although the infiltrated water is evenly distributed in the fracture outcrops, the movement of water inside the fractures totally differs in both the horizontal and the vertical directions. In the range of the red dashed area of Fig. 8d, the apparent resistivity is about $1000\Omega m$. Compared with the lower-resistivity area, it still shows higher resistivity even though the fracture medium reached saturation. Therefore, we infer that the internal structure should be categorized as case 4; that is, it may be an open fracture.

It is notable that the resistivity close to the intersection point is substantially lower than that

elsewhere. In comparison with Fig. 8a, the injected water obviously tends to percolate at the intersection point (Fig. 8b). Thus, taking the intersection point as the vertex, an inverted funnel-like area with lower resistivity is formed. This phenomenon indicates that fluid prefers to flow along the dominant pathways around the intersection point. With regard to its temporal variation, the resistivity gradually decreases with the continuous invasion and expansion of infiltrating water. The blue area (lower resistivity) features an expanding trend, and the preferential flow, which is revealed by the dominant pathways, becomes more obvious. The inverted funnel-like area increases during the early stage of infiltration and then tends toward an approximately steady state after approximately 13 h (as shown in Fig. 8d). Subsequently, previously infiltrated water fills the available storage space. Assuming that the resistivity variation was exclusively the result of water content changes within the medium, these figures clearly reveal the possible variations in the water content. The area with a higher infiltration capacity expands gradually in the upper center of the fractures rather than the fracture boundaries over time. Hence, it could be argued that the region adjacent to the intersection has better hydraulic conductivity. In fact, our field observation has proven that this region had wider gaps, and these gaps of the crossing fractures become dominant pathways for water infiltration.

Heterogeneous Infiltration: As explained above, we can extrapolate the structural heterogeneity of single fractures from the results of the relative variation in resistivity. These results further illustrate the infiltration process of a water body in field experiments. In particular, a quasi three-dimensional distribution for the crossing fractures is initially developed.

As shown in Fig. 8f–h, resistivity tends to decrease gradually in the vertical direction, especially in the region which has wider gaps. A possible reason is that during the infiltration process, water preferentially infiltrates and moves swiftly along channels with better hydraulic conductivity, whereas water tends not to move through channels with poor hydraulic conductivity. Another factor may be the drainage effect on water movement. Zhou et al. (2004) reported that the heterogeneity of water

drainage and air invasion might have a significant effect on the fracture network by exposing the rock to oxidizing conditions. With the drainage of infiltrated water, any air that fails to escape is sealed in a narrow fracture space composed of dense surrounding rock. The air pressure increases continuously with the infiltration time, and the porosity of the filling materials increases, thus reducing the overall permeability of the medium. It can therefore be concluded that the heterogeneous infiltration within the fractures is intricately related to the structural difference, whether the factor is dominant pathways or drainage effects.

The results of both single fracture and crossing fracture experiments showed similar characteristics. That is, the infiltration fronts show a wave-like shape near the fractures at the ground surface in the initial stage of infiltration, and the fronts at different depths vary with infiltration time. In contrast, the deep areas near the boundary induce weaker electrical responses, and the variation rate of resistivity is close to zero. These results suggest the following: (1) Widespread preferential flow has an important impact on fluid transport during infiltration. (2) The electrical characteristics of different regions reflect the spatial complexity of fracture structures. (3) The relative variation in resistivity distribution can be used to evaluate the heterogeneous infiltration of single fractures.

5.2. Preferential Infiltration Process in the Fractures Revealed by FT-ERT

5.2.1 The Single Fracture

Dumont et al. (2018) confirmed that it is feasible to convert resistivity into water content and depicted the infiltration front by the relative change in resistivity. In this section, we attempt to calculate the velocity and estimate the permeability of the single fracture by the FT-ERT results. According to Eq. 1, the resistivity of the fractured medium will decrease when encountering water, while the resistivity of the unsaturated part remains unchanged. This electrical response characteristics are helpful to determine the spatial distribution of the infiltration fronts. Meanwhile, in Sect. 5, the relative variation in resistivity has been shown to reveal the infiltration process and

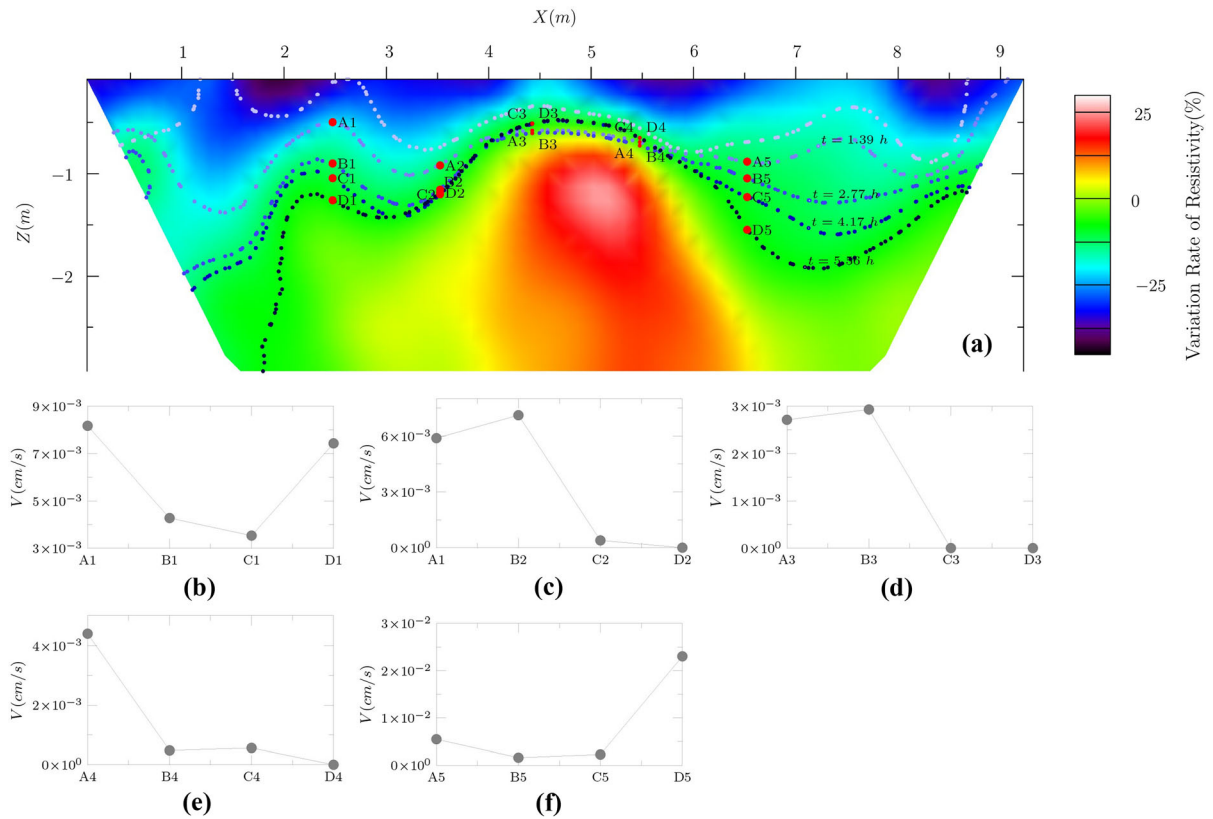


Figure 10

Results of the infiltration fronts and instantaneous velocity variations estimated by the electrical response characteristics. **a** Distribution of water infiltration fronts; **b** velocity at A1, B1, C1 and D1 ($x = 2.5m$); **c** velocity at A2, B2, C2 and D2 ($x = 3.5m$); **d** velocity at A3, B3, C3 and D3 ($x = 4.5m$); **e** velocity at A4, B4, C4 and D4 ($x = 5.5m$); **f** velocity at A5, B5, C5 and D5 ($x = 6.5m$)

the advancing fronts. Therefore, an isoline with a relative variation of 0 here is considered to be the advancing front. On this basis, quantitative analysis can be adopted to calculate the infiltration velocity, and then evaluate the hydraulic conductivity within the single fracture.

Velocity Calculation: The advancing velocity of the infiltration front can be obtained by comparing the changes in the infiltration front at different times using two neighboring points in the vertical direction of fluid flow. For example, point A and point B are two neighboring points (shown in Fig. 10a) on the contour lines at $t = t_1$ and $t = t_2$, respectively. The mean velocity V_m of point B can be obtained by

$$V_m = \frac{L_B}{t_2}, \quad (7)$$

where L_B is the displacement of the fluid from the

surface to point B at the initial infiltration time ($t_0 = 0$). The instantaneous velocity V_i of point B can be obtained by

$$V_i = \frac{\Delta L}{(t_2 - t_1)}, \quad (8)$$

where ΔL is the vertical displacement from A to B, i.e., $\Delta L = L_B - L_A$.

In this way, we selected five representative points of the single fracture to calculate the velocity at different times. Figure 10a shows the spatial distribution of these points on five isolines, which represent different times from light blue to dark blue. The selected points A_i , B_i , C_i and D_i ($i = 1, 2, 3, 4, 5$) in this figure have the same horizontal coordinates, but come from different depths. To analyze the variation in the velocity with depth, we extracted the instantaneous velocity at the corresponding times at

the positions of $x = 2.5m$, $x = 3.5m$, $x = 4.5m$, $x = 5.5m$ and $x = 6.5m$ (Fig. 10b–f). Figure 10b shows the instantaneous velocity of water at A1, B1, C1 and D1. The velocity at A1 was $8.2 \times 10^{-3} cm/s$, which decreased to $4.3 \times 10^{-3} cm/s$ with increasing infiltration at C1 and then increased to $7.4 \times 10^{-3} cm/s$ at D1. These sharp changes in velocity reflect the anisotropy of hydraulic conductivity. The same fluctuation can also be observed in Fig. 10f. The instantaneous velocity in the period of $t_3 = 2.77h$ to $t_4 = 4.17h$ is less than that in the period of $t_4 = 4.17h$ to $t_5 = 5.56h$. We can infer that the infiltrated water expands downward rapidly, and this area has better hydraulic conductivity. In contrast, as shown in Fig. 10c–e, the instantaneous velocity demonstrates a decreasing trend. During the period of t_4 to t_5 , the instantaneous velocity decreased significantly, almost to 0 cm/s, and the infiltration process was close to stagnation. For instance, water swiftly moved to B2 from A2, and the velocity increased slightly but subsequently decreased at C2 and D2. These

variation characteristics of the instantaneous velocity are also illustrated in points of C3, D3 and C4, D4. The velocity variation curves show that the infiltration process in the single fracture is nonlinear and preferential. The distribution of velocity within the single fracture is different due to the heterogeneity.

Permeability estimation

In order to elucidate the heterogeneity of single fractures and further interpret the hydraulic characteristics within the interior of the fractured medium, we estimated the permeability on the basis of velocity results. When the infiltration reaches a steady state, the hydraulic gradient of infiltration in the vertical direction is approximately 1. Thus, the velocity is the hydraulic conductivity of the fracture at this time and is therefore determined accordingly. Figure 11 plots the instantaneous and mean velocity curves calculated at four different times. In general, once the fractured medium is saturated, the mean velocity should be close to the instantaneous velocity (gray coverage area in Fig. 11). Consequently, the velocity

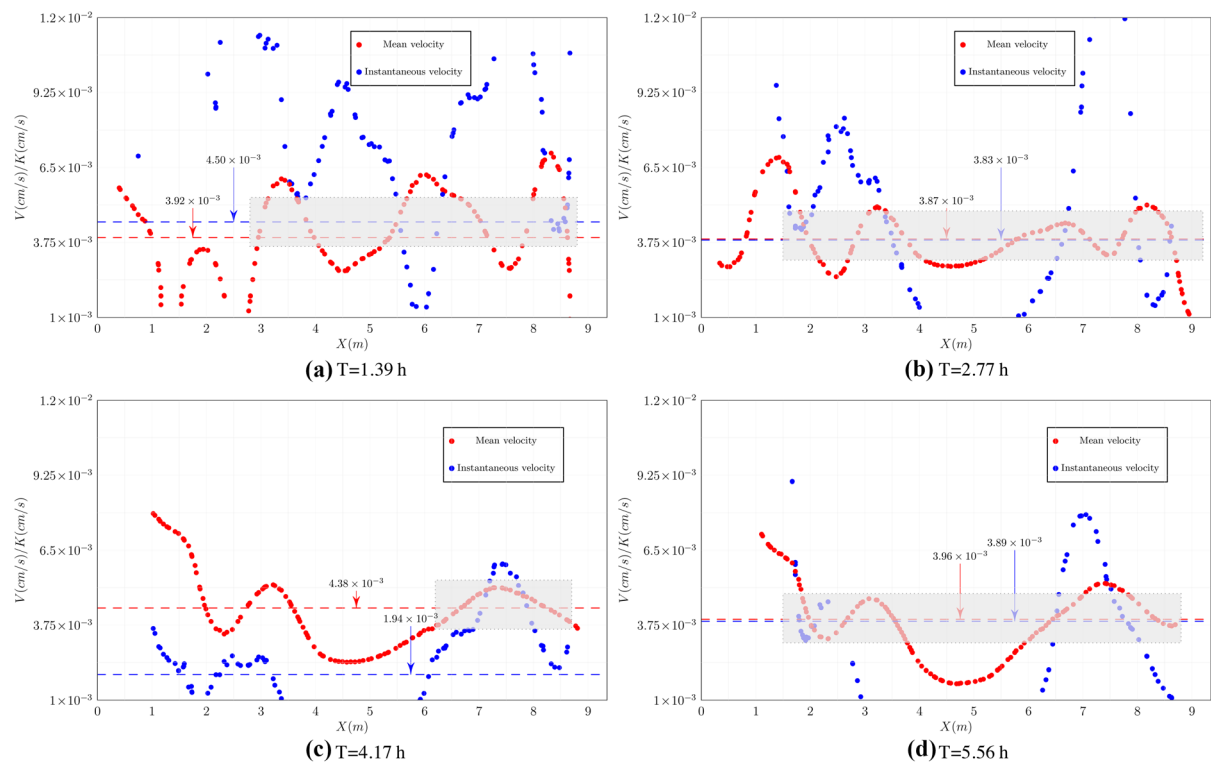


Figure 11
Mean velocity and instantaneous velocity curves

between the mean velocity (red dots) and the instantaneous velocity (blue dots) in Fig. 11 can be given as the apparent hydraulic conductivity of the fractured medium. We unexpectedly discovered that the average of the instantaneous velocity (blue parallel dashed lines) and the average of the mean velocity (red parallel dashed lines) were very close except in Fig. 11c. The velocity difference shown in Fig. 11c indicates that the infiltration has not yet reached a steady state. The relative error between the mean velocity and the instantaneous velocity is 125.77%. Such a large error is not suitable for parameter estimation. However, we can choose a steady state to estimate the permeability in Fig. 11b as an example. The average values of the mean velocity and the instantaneous velocity (red and blue parallel dashed lines in this figure) at $t = 2.77h$ are $3.87 \times 10^{-3} cm/s$ and $3.83 \times 10^{-3} cm/s$, respectively. The relative error of these two velocities is 1.03%. Then we can estimate that the hydraulic conductivity is 3.33 m/day by using their average value. In this way, the permeability can be estimated as $3.50 \times 10^{-12} m^2$. This suggests that the FT-ERT method is feasible for evaluating the hydraulic characteristics of the single fracture in a steady state.

5.2.2 The Crossing Fractures

In the same way, we also estimated the hydraulic conductivity and the permeability of the crossing fractures. It can be seen that the infiltration process reached a steady state at $t = 13.1h$ in Fig. 8. The mean velocity is $1.30 \times 10^{-3} cm/s$ and the

instantaneous velocity is $1.18 \times 10^{-3} cm/s$. With a relative error of 9.02%, we estimated the hydraulic conductivity, which is 1.07 m/day, and the corresponding permeability is $1.13 \times 10^{-12} m^2$. Table 1 lists the estimated hydraulic parameters of our two monitoring experiments by FT-ERT. We calculated the velocity at different times and estimated the hydraulic parameters. Compared with the single fracture, the crossing fractures have lower hydraulic conductivity and permeability. This is consistent with the field observations. The single fracture is subject to extensive weathering, with a larger gap filled with sand and clay, and the crossing fractures are less effected by weathering. Fracture surfaces are in close contact. The infiltration water volume and percolation velocity are less than those of the single fracture.

During the field experiment, we drilled a borehole to conduct a sampling analysis of the filling materials and the rock matrix constituting the crossing fractures. The results of the core sample analysis revealed that the surrounding rock is a biotite plagioclase gneiss with porosity ranging from 1.2% to 4.7% and permeability of $5.56 \times 10^{-18} m^2$, which indicates that the surrounding rock has a limited effect on the fluid migration of single fractures. In contrast, the filling material is medium fine sand with a particle size range of $0.16 \sim 0.42 mm$ and is mixed with a small amount of clay. The porosity of the filling materials ranges from 16% to 38%. Based upon the physical properties of the fractured medium, we can infer that the physical properties of the filling materials in the crossing fractures are similar to those of fine sand. Additionally, the estimated hydraulic conductivity of

Table 1

The infiltration velocity and estimated hydraulic parameters obtained by FT-ERT

Number	V_m (cm/s)	V_i (cm/s)	Relative error (%)	K (m/d)	k (m^2)
SF1	3.92×10^{-3}	4.50×10^{-3}	14.80	3.64	3.82×10^{-12}
SF2	3.87×10^{-3}	3.83×10^{-3}	1.03	3.33	3.50×10^{-12}
SF3	1.94×10^{-3}	4.38×10^{-3}	125.77	2.73	2.87×10^{-12}
SF4	3.96×10^{-3}	3.89×10^{-3}	1.77	3.39	3.56×10^{-12}
CF1	1.28×10^{-3}	1.13×10^{-3}	11.77	1.04	1.09×10^{-12}
CF2	0.79×10^{-3}	0.69×10^{-3}	12.52	0.64	6.72×10^{-13}
CF3	1.30×10^{-3}	1.18×10^{-3}	9.02	1.07	1.13×10^{-12}

Note: SF1, SF2, SF3, and SF4 are the selected points of the single fracture at $t = 1.39h$, $t = 2.77h$, $t = 4.17h$, and $t = 5.56h$, respectively. CF1, CF2, and CF3 are the selected points of the crossing fractures at $t = 7.5h$, $t = 8.6h$ and $t = 13.1h$, respectively

the single fracture and the crossing fractures are $K_{sf} = 3.3m/d$ and $K_{cf} = 1.0m/d$. The estimated hydraulic conductivity results are consistent with the results of a pumping test ($K_p = 3.28m/d$) and a surface infiltration test ($K_i = 2.74m/d$) at the experimental site. Our results accord with those of the pumping test and surface infiltration test at the meter (or finer) scale.

Considering factors such as fracture morphology and networks, the hydraulic parameters of fractured medium have more complexity and uncertainty in different scales. It is very difficult to obtain information about the internal structure and hydraulic parameters of single fractures buried in the subsurface. Moreover, the migration of infiltration into the interior of fractures is also intensely affected by its structural heterogeneity. Under this premise, the FT-ERT method not only distributes the structural heterogeneity of single fractures underground, but also offers excellent prediction and estimation capability to determine the hydraulic parameters.

6. Conclusion

Based on experiments conducted on fractures within granite bedrock, we investigated the effectiveness of the FT-ERT method in characterizing the conductivity and preferential flow of a fractured medium. We first established and verified the validity of the numerical model and forward calculation of the fracture. Then, the spatial distribution of resistivity in the fracture was obtained through in situ infiltration monitoring and data analysis. Correspondingly, the inversion results from the original data reflect that the interior of the fracture has a completely different resistivity distribution. Considering the contact relationship between the two rock surfaces and the properties of the filling materials, we analyzed the reason for the large differences in resistivity. We also analyzed and verified the mechanism responsible for preferential flow within the fractures by implementing time-lapse FT-ERT.

The FT-ERT method has advantages in evaluating the spatial permeability distribution of the fracture. Fractures in the field are generally distributed unevenly; accordingly, the fracture size, fracture

structure, surrounding rock properties, contact conditions, and other factors differ in space and thus are not known. On the basis of fluid flow in fractures, this method is able not only to monitor the static spatial distribution of resistivity inside fractures but also to easily implement dynamic monitoring. Since the flow of fluid through a fractured medium occurs mainly between water-conducting fracture networks, the fluid flow process monitored by the FT-ERT method can indirectly explain the spatial distribution characteristics of the water-conducting fracture network and its effect on the fluid flow process. Therefore, the FT-ERT method is of great benefit for exploring the saturation and unsaturation of fractured rock masses, studying the interaction process between water and rocks, and estimating the hydrometric parameters of fractured medium.

Considering the above advantages, this method could be applied to other types of engineering infrastructures, especially to investigate repositories for buried or stored nuclear waste and fractured rock sites that have been contaminated as a result of past disposal or other practices.

Acknowledgements

This study was supported by the National Natural Science Foundation of China [No. 41172208], the nuclear waste geological disposal project of COST-IND [2012-493], Nanjing University Innovation and Creative Program for PhD Candidate [No. CXCXY19-58], the Science and Technology Support Program [2014BAK16B01], and the National Natural Science Foundation of China [No. 41702247]. Thanks to S. A. Junejo for valuable advice concerning the manuscript.

Author contributions ZS: formal analysis and investigation, methodology, writing—original draft preparation; Q-YZ: conceptualization, software, funding acquisition; D-BL: supervision, writing—review and editing; SX: methodology, software.

Availability of data and material

The data that support the findings of this study are available from the corresponding author upon reasonable request.

Declarations

Conflict of interest The authors declare that they have no known competing financial interests or personal relationships that could have appeared to influence the work reported in this paper.

Code availability The programs utilized in this study are available from <http://ertcenter.nju.edu.cn/> after an application.

Publisher's Note Springer Nature remains neutral with regard to jurisdictional claims in published maps and institutional affiliations.

REFERENCES

- Abdelazim, R. (2016). An integrated approach for relative permeability estimation of fractured porous media: laboratory and numerical simulation studies. *Journal of Petroleum Exploration and Production Technology*. <https://doi.org/10.1007/s13202-016-0250-x>.
- Andrade, R., & Rangarajan, R. (2019). Transient resistivity response to infiltrating water front through vadose zone. *HydroResearch*, 2, 1–9. <https://doi.org/10.1016/j.hydres.2019.11.001>.
- Archie, G.E. (1942). The electrical resistivity log as an aid in determining some reservoir characteristics. *Transactions of the AIME*, 146, 54–62. <https://doi.org/10.2118/942054-G>.
- Binley, A., & Kemna, A. (2005). DC resistivity and induced polarization methods. *Hydrogeophysics* (pp. 129–156). Springer. https://doi.org/10.1007/1-4020-3102-5_5.
- Bodin, J., Delay, F., & de Marsily, G. (2003). Solute transport in a single fracture with negligible matrix permeability: 1. Fundamental mechanisms. *Hydrogeology Journal*, 11(4), 418–433. <https://doi.org/10.1007/s10040-003-0268-2>.
- Brooks, R. H., & Corey, A. T. (1966). Properties of porous media affecting fluid flow. *Journal of the Irrigation and Drainage Division*, 92(2), 61–90.
- Dumont, G., Pilawski, T., Hermans, T., Nguyen, F., & Garré, S. (2018). The effect of initial water distribution and spatial resolution on the interpretation of ert monitoring of water infiltration in a landfill cover. *Hydrology and Earth System Sciences Discussions*, 2018, 1–26. <https://doi.org/10.5194/hess-2018-163>.
- Fredlund, D. G., & Xing, A. Q. (1994). Equations for the soil-water characteristic curve. *Canadian Geotechnical Journal*, 31(4), 521–532. <https://doi.org/10.1139/t94-061>.
- Glover, P., Zadjali, I., & Frew, K. (2006). Permeability prediction from micp and nmr data using an electrokinetic approach. *Geophysics*, 71(4), 49–60.
- Günther, T., Rücker, C., Spitzer, K., et al. (2006). 3-d modeling and inversion of dc resistivity data incorporating topography-part II: inversion. *Geophysical Journal International*, 166(2), 506–517.
- Hadgu, T., Karra, S., Kalinina, E., Makedonska, N., Hyman, J. D., Klise, K., et al. (2017). A comparative study of discrete fracture network and equivalent continuum models for simulating flow and transport in the far field of a hypothetical nuclear waste repository in crystalline host rock. *Journal of Hydrology*, 553, 59–70. <https://doi.org/10.1016/j.jhydrol.2017.07.046>.
- Herron, M. M. (1988). Geochemical classification of terrigenous sands and shales from core or log data. *Journal of Sedimentary Research*, 58(5), 820–829.
- Houseworth, J. E., Asahina, D., & Birkholzer, J. T. (2013). An analytical model for solute transport through a water-saturated single fracture and permeable rock matrix. *Water Resources Research*, 49(10), 6317–6338. <https://doi.org/10.1002/wrcr.20497>.
- Huang, J., Christ, J., & Goltz, M. N. (2021). Analytical solutions for contaminant fate and transport in parallel plate fracture-rock matrix systems with poiseuille flow. *Journal of Hydrology*, 596, 126097. <https://doi.org/10.1016/j.jhydrol.2021.126097>.
- Hyman, J. D., Jiménez-Martínez, J., Gable, C. W., Stauffer, P. H., & Pawar, R. J. (2019). Characterizing the impact of fractured caprock heterogeneity on supercritical CO₂ injection. *Transport in Porous Media*, 131(3), 935–955. <https://doi.org/10.1007/s11242-019-01372-1>.
- Kuhlman, K. L., Malama, B., & Heath, J. E. (2015). Multiporosity flow in fractured low-permeability rocks. *Water Resources Research*, 51(2), 848–860. <https://doi.org/10.1002/2014WR016502>.
- LaBrecque, D. J., Sharpe, R., Wood, T., & Heath, G. (2004). Small-scale electrical resistivity tomography of wet fractured rocks. *Ground Water*, 42(1), 111–118.
- Loke, M. H., Chambers, J. E., Rucker, D. F., Kuras, O., & Wilkinson, P. B. (2013). Recent developments in the direct-current geoelectrical imaging method. *Journal of Applied Geophysics*, 95(C), 135–156. <https://doi.org/10.1016/j.jappgeo.2013.02.017>.
- Lu, D., Huang, D., & Xu, C. (2021). Estimation of hydraulic conductivity by using pumping test data and electrical resistivity data in faults zone. *Ecological Indicators*, 129, 107861. <https://doi.org/10.1016/j.ecolind.2021.107861>.
- MacNeill, J. (1980). *Electrical conductivity of soils and rocks*. Geonics Limited.
- Nasseri, M. H. B., Grasselli, G., & Mohanty, B. (2010). Fracture toughness and fracture roughness in anisotropic granitic rocks. *Rock Mechanics and Rock Engineering*, 43(4), 403–415. <https://doi.org/10.1007/s00603-009-0071-z>.
- Nimmer, R. E., Osiensky, J. L., Binley, A. M., Sprenke, K. F., & Williams, B. C. (2007). Electrical resistivity imaging of conductive plume dilution in fractured rock. *Hydrogeology Journal*, 15(5), 877–890. <https://doi.org/10.1007/s10040-007-0159-z>.
- Noiriél, C., Gouze, P., & Madé, B. (2013). 3D analysis of geometry and flow changes in a limestone fracture during dissolution. *Journal of Hydrology*, 486, 211–223. <https://doi.org/10.1016/j.jhydrol.2013.01.035>.
- Ochs, J., & Klitzsch, N. (2020). Considerations regarding small-scale surface and borehole-to-surface electrical resistivity tomography. *Journal of Applied Geophysics*, 172, 103862. <https://doi.org/10.1016/j.jappgeo.2019.103862>.

- Osipov, A. A. (2017). Fluid mechanics of hydraulic fracturing: a review. *Journal of Petroleum Science and Engineering*, 156, 513–535. <https://doi.org/10.1016/j.petrol.2017.05.019>.
- Rashid, F., Glover, P. W. J., Lorinczi, P., Hussein, D., Collier, R., & Lawrence, J. (2015). Permeability prediction in tight carbonate rocks using capillary pressure measurements. *Marine and Petroleum Geology*, 68, 1–15. <https://doi.org/10.1016/j.marpetgeo.2015.10.005>.
- Robinson, J., Slater, L., Johnson, T., Shapiro, A., Tiedeman, C., Ntarlagiannis, D., et al. (2016). Imaging pathways in fractured rock using three-dimensional electrical resistivity tomography. *Ground Water*, 54(2), 186–201. <https://doi.org/10.1111/gwat.12356>.
- Ronczka, M., Rücker, C., & Günther, T. (2015). Numerical study of long-electrode electric resistivity tomography – accuracy, sensitivity, and resolution. *Geophysics*, 80(6), 317–328. <https://doi.org/10.1190/geo2014-0551.1>.
- Rücker, C., Günther, T., & Spitzer, K. (2006). 3-d modeling and inversion of dc resistivity data incorporating topography-part I: modeling. *Geophysical Journal International*, 166(2), 495–505.
- Sahimi, M. (2011). *Flow and transport in porous Media and fractured rock: from classical methods to modern approaches*. John Wiley & Sons.
- Song, Z., & Zhou, Q. Y. (2019). Micro-scale granite permeability estimation based on digital image analysis. *Journal of Petroleum Science and Engineering*, 180, 176–185. <https://doi.org/10.1016/j.petrol.2019.05.037>.
- Sreeparvathy, V., Kambhammettu, B. V. N. P., Peddinti, S. R., & Sarada, P. S. L. (2019). Application of ert, saline tracer and numerical studies to delineate preferential paths in fractured granites. *Groundwater*, 57(1), 126–139. <https://doi.org/10.1111/gwat.12663>.
- Suri, Y., Islam, S. Z., & Hossain, M. (2020). Effect of fracture roughness on the hydrodynamics of proppant transport in hydraulic fractures. *Journal of Natural Gas Science and Engineering*, 80, 103401. <https://doi.org/10.1016/j.jngse.2020.103401>.
- Suski, B., Rizzo, E., & Revil, A. (2004). A sandbox experiment of self-potential signals associated with a pumping test. *Vadose Zone Journal*, 3(4), 1193–1199.
- Tarantola, A., & Valette, B. (1982). Generalized nonlinear inverse problems solved using the least squares criterion (paper 1R1855). *Reviews of Geophysics and Space Physics*, 20, 219–240.
- Tayfun, Babadagli, Xiaojuan, Ren, & Kayhan, Develi. (2015). Effects of fractal surface roughness and lithology on single and multiphase flow in a single fracture: an experimental investigation. *International Journal of Multiphase Flow*, 68(C), 40–58. <https://doi.org/10.1016/j.ijmultiphaseflow.2014.10.004>.
- Travelletti, J., Sailhac, P., Malet, J. P., Grandjean, G., & Ponton, J. (2011). Hydrological response of weathered clay-shale slopes: water infiltration monitoring with time-lapse electrical resistivity tomography. *Hydrological Processes*, 26(14), 2106–2119. <https://doi.org/10.1002/hyp.7983>.
- Tsang, C.-F., & Doughty, C. (2003). Multirate flowing fluid electric conductivity logging method. *Water Resources Research*, 39(12), 1354.
- Uhlemann, S., Wilkinson, P. B., Chambers, J. E., Maurer, H., Merritt, A. J., Gunn, D. A., & Meldrum, P. I. (2015). Interpolation of landslide movements to improve the accuracy of 4D geoelectrical monitoring. *Journal of Applied Geophysics*, 121, 93–105. <https://doi.org/10.1016/j.jappgeo.2015.07.003>.
- van Genuchten, M. T. (1980). A closed-form equation for predicting the hydraulic conductivity of unsaturated soils1. *Soil Science Society of America Journal*, 44(5), 892. <https://doi.org/10.2136/sssaj1980.03615995004400050002x>.
- Walton, W. C. (1990). *Groundwater pumping tests*. CRC Press.
- Wang, H. (2019). Hydraulic fracture propagation in naturally fractured reservoirs: complex fracture or fracture networks. *Journal of Natural Gas Science and Engineering*, 68, 102911–20. <https://doi.org/10.1016/j.jngse.2019.102911>.
- Wang, J., Chen, L., Su, R., & Zhao, X. (2018). The Beishan underground research laboratory for geological disposal of high-level radioactive waste in China: planning, site selection, site characterization and in situ tests. *Journal of Rock Mechanics and Geotechnical Engineering*, 10(3), 411–435. <https://doi.org/10.1016/j.jrmge.2018.03.002>.
- Yan, X., Qian, J., Ma, L., Wang, M., & Hu, A. (2018). Non-fickian solute transport in a single fracture of marble parallel plate. *Geofluids*, 2018(5), 1–9. <https://doi.org/10.1155/2018/7418140>.
- Zambrano, M., Pitts, A. D., Salama, A., Volatili, T., Giorgioni, M., & Tondi, E. (2019). Analysis of fracture roughness control on permeability using sfm and fluid flow simulations: implications for carbonate reservoir characterization. *Geofluids*, 2019, 4132386. <https://doi.org/10.1155/2019/4132386>.
- Zhou, Q. Y., Matsui, H., & Shimada, J. (2004). Characterization of the unsaturated zone around a cavity in fractured rocks using electrical resistivity tomography. *Journal of Hydraulic Research*, 42(sup1), 25–31. <https://doi.org/10.1080/00221680409500044>.
- Zhou, Q. Y., Shimada, J., & Sato, A. (1999). Three-dimensional soil resistivity inversion using patching method. *Journal of the Japan Society of Engineering Geology*, 39(6), 524–532. <https://doi.org/10.5110/jjseg.39.524>.
- Zou, L., Jing, L., & Cvetkovic, V. (2017). Modeling of solute transport in a 3D rough-walled fracture-matrix system. *Transport in Porous Media*, 116(3), 1005–1029. <https://doi.org/10.1007/s11242-016-0810-z>.